# RHESSI Images and spectra of two small flares

L. Maltagliati and  A. Falchi
*Osservatorio Astrofisico di Arcetri, L. Fermi 5, I-50125 Firenze, Italy*

L. Teriaca
*Max-Planck-Institut für Sonnensystemforschung Max-Planck-Str. 2, 37191 Katlenburg-Lindau, Germany*

**Abstract.** We studied the evolution of two small flares (GOES class C2 and C1) that developed in the same active region with different morphological characteristics: one is extended and the other is compact. We analyzed the accuracy and the consistency of different algorithms implemented in RHESSI software to reconstruct the image of the emitting sources, for energies between 3 and 12 keV. We found that all tested algorithms give consistent results for the peak position while the other parameters can differ at most by a factor 2. *Pixon* and *Forward-fit* generally converge to similar results but *Pixon* is more reliable for reconstructing a complex source. We investigated the spectral characteristics of the two flares during their evolution in the 3 – 25 keV energy band. We found that a single thermal model of the photon spectrum is inadequate to fit the observations and we needed to add either a non-thermal model or a hot thermal one. The non-thermal and the double thermal fits are comparable. If we assume a non-thermal model, the non-thermal energy is always higher than the thermal one. Only during the very final decay phase a single thermal model fits fairly well the observed spectrum.

## 1. Introduction

Since February 2002, the RHESSI (Reuven Ramaty High-Energy Spectroscopic Imager) satellite carries out X-ray and $\gamma$-ray observations of flares and other forms of solar magnetic activity (Lin et al., 2002). In particular, the 3 – 25 keV spectral band is of great relevance. It is comprehensive of the thermal and non-thermal domain of the bremsstrahlung, giving us information about the energy deposition of the particles accelerated in the impulsive phase. The low-energy non-thermal electrons are especially crucial in small events and in microflares. Besides, a broadened emission line feature at around 6.7 keV, mainly due to Fe ions, and a weaker line feature at around 8 keV due to Fe and Ni ions are observable and can give information on electron distributions different from the ones obtained from the bremsstrahlung continuum. The X-ray band 3 – 25 keV is observed by RHESSI with unprecedented spectral resolution (1 keV) and imaging capability (2.3″). Moreover, when both attenuators are out, RHESSI has a much larger effective area than any earlier instrument, providing information on low-level energy releases with much higher sensitivity.

These RHESSI characteristics allow extensive studies of microflares related to both imaging and spectra (among others: Krucker et al., 2002, Benz and Grigis, 2002, Krucker and Hudson, 2004, Hannah et al., 2004, Liu et al., 2004). Images at low energy of these small events are generally reconstructed using the *Clean* algorithm available in RHESSI software (Hurford et al., 2002, Schwartz et al., 2002). In fact, in this process of image reconstructions, *Clean*, together with *Pixon* (Metcalf et al., 1996) and *Forward-fit* (Aschwanden et al., 2002), converge to the best solutions for a simple source morphology and the photometric accuracy seems to be uniform in different energy ranges higher than 10 keV (Aschwanden et al., 2004). It may be of interest to test the photometric accuracy and the consistency of the image reconstruction algorithms for more complex sources and lower energies.

It seems quite established that at the peak time of a flare the observed spectra up to $\approx 10$ keV can be fitted with a single thermal model (T $\approx 10$ MK) of the photon spectrum. At higher energies a good fit can be obtained adding a non-thermal bremsstrahlung emission with energy cutoff below 10 keV and a power-law index $\gamma$ between 5 and 8, meaning that the spectra of small flares are usually softer than the ones of large flares. Benz and Grigis (2002) obtained a good fit of a microflare spectrum at the maximum phase also adding a second thermal component with higher temperature (T$\approx 25$ MK), but they reject this interpretation because this hotter component is no more present during the cooling and then the behaviour of the photons higher than 10 keV is more consistent with the standard flare scenario of precipitating non-thermal electrons. During the decay phase instead, the spectra can be fitted either with a thermal component only (Liu et al., 2004) or with a non-thermal component with an index $\gamma \approx 10$ (Krucker et al., 2002, Hannah et al., 2004). Therefore it is very important to study the behaviour of the spectra of small flares during their evolution in order to investigate if the hardness of the spectrum changes with time, as can be observed in larger flares that show a direct correlation between the hard X-ray flux and the spectral hardness (Fletcher and Hudson, 2002, Hudson and Fárník, 2002, Grigis and Benz, 2004).

In this paper we present a study on the morphological and spectral properties of two small flares (GOES class C2 and C1) in the energy range 3 – 25 keV. In particular we compare the image reconstruction algorithms to carefully check the characteristics of these two events at these low energies, when both attenuators are out, and we investigate how their X-ray spectrum evolves with time.

## 2. Observations

An observing campaign coordinated between ground and space based instruments was planned to observe flare events, sampling the solar atmosphere from the chromosphere to the corona. Monochromatic images at several wavelengths, in the continuum and within the Hα line have been acquired by means of the tunable Universal Birefringent Filter (UBF) and the Zeiss filter at the Dunn Solar Tower of the National Solar Observatory (NSO) / Sacramento Peak. The field of view (FOV) is of about $150'' \times 150''$ with a spatial scale of $0.5'' \times 0.5''$ and a temporal cadence of few seconds. Spectra have been acquired with the Horizontal Spectrograph in 3 chromospheric lines (Ca II K, He I D3 and Hγ), with a temporal cadence of 4 s. Simultaneously, spectroheliograms of the same region were obtained in transition region and coronal lines with the Coronal Diagnostic Spectrometer (CDS) aboard SOHO (Harrison et al., 1995). During this campaign we observed the region NOAA AR 10061 (N10W20) on 2002 August 11 from 14:00 to 19:00 UT. Two homologous flares (GOES class C2 and C1) developed in this region around 14:40 UT and 16:25 UT. In this paper we mainly concentrate on the diagnostic provided by RHESSI in conjunction with Hα data. The flare dynamics, using also spectra from NSO and CDS, will be analyzed in a later paper.

The image of the whole active region at 14:41:47 UT (Figure 1), acquired with the HASTA telescope (San Juan, Argentina) in the blue wing of Hα line, shows the two ribbons developed during the first flare. Unfortunately the FOV of the UBF (indicated in Figure 1 by the white box) includes only the western ribbon of the flare.

In Figure 2 we show the high resolution images obtained with UBF in the Hα line center during the two flares. Both flares have the characteristics of eruptive two-ribbon flares and are indeed triggered by the eruption of different portions of the same filament. However they exhibit very different morphologies. The upper panels show that the upper eastern part of the filament disappears at 14:14:57 UT. The emission maximum of the western ribbon is reached at 14:41:48 UT when two extended parallel ribbons developed in NE-SW direction (see Figure 1), at the two sides of the filament. MDI/SOHO (Scherrer et al., 1995) full disk magnetogram taken at 14:27:34 UT is used to determine the position of the apparent magnetic neutral line and the alignment, done using MDI and UBF continuum, is estimated to be within $1''$. The neutral line follows very well the filament and the ribbon positions hint at a system of large coronal loops ($\approx 70\,000$ km) in East-West direction. Bottom panels show that at 16:00:16 UT the emission from the first episode has almost disappeared and the whole filament is visible. At
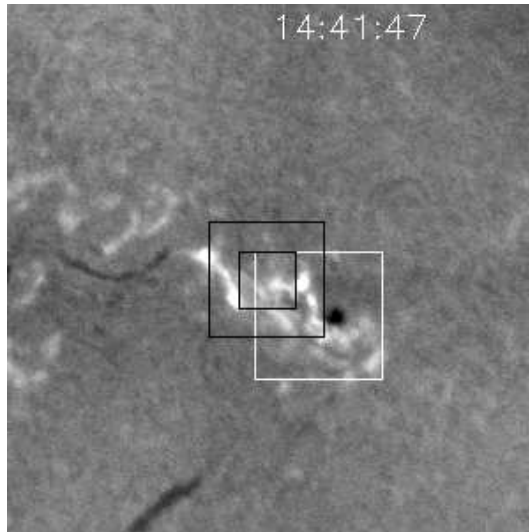
3

*Figure 1.* Image of the active region NOAA AR 10061 acquired by the HASTA telescope in the blue wing of Hα, approximately at the peak time of the first flare (West at right, North at top). Two bright ribbons are clearly visible. The white box $(150'' \times 150'')$, that includes only one ribbon, indicates the FOV of the UBF/National Solar Observatory. The black boxes indicate the FOV used for RHESSI image reconstruction (see Sec. 3).

16:31 UT very compact ribbons develop nearby the central part of the filament, suggesting the presence of stressed and lower loops. At 17:13:31 UT the filament structure is again in the pre-flare conditions.

Figure 3 shows the light curves of the two events observed in soft X-rays at $1 - 8$ Å by GOES, in the energy bins $3 - 6$ and $12 - 25$ keV by RHESSI and in Hα line center by UBF. We notice that GOES recorded a C1 flare at about 15:50 UT which did not occur in the observed active region, and that GOES and UBF light curves are very similar for the two studied flaring episodes. RHESSI was in its night during the impulsive phase of the first event and acquired data only during its decay phase. For the second event RHESSI exited from its night just after the very first spike at 16:25:54 UT, well visible in the Hα curve, missing the beginning of the impulsive phase. The significant increase of the counts in the time interval 14:56 UT - 15:12 UT, at energies higher than 10 keV, is due to charged particle precipitation event and then the data in this time interval cannot be considered. RHESSI had both thin and thick attenuators out for the whole time interval.
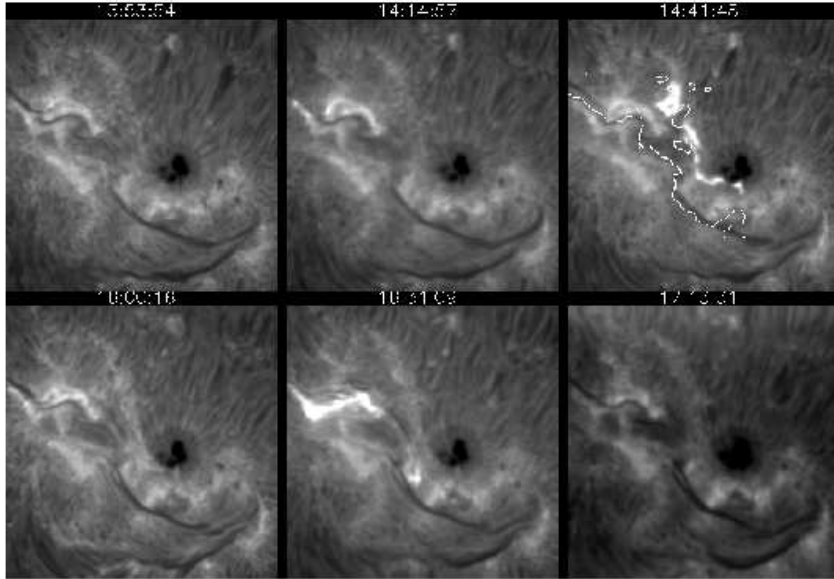
4

*Figure 2.* Evolution of the two flares. Images have been acquired with UBF at the center of Hα line. In the upper right panel the white line indicates the apparent magnetic neutral line obtained from MDI/SOHO data. At 14:41:48, the time of the maximum of the first flare, only one ribbon is within the FOV (see Figure 1). At 16:31:09 UT, the peak time of the second flare, the ribbons follow the underlying filament and appear very close to each other.

## 3.   RHESSI Image Reconstruction

In RHESSI software 5 different algorithms have been implemented to reconstruct images from the 'back projection' map, which contains sidelobes due to the modulation pattern of the collimators. Aschwanden et al. (2004) carried out a comparative study on the accuracy of the algorithms between 10 and 60 keV for a strong flare with two resolved sources. We did analyze the efficiency and the accuracy of different algorithms in the energy range $3 - 25$ keV when both thin and thick attenuators are out and for two different source morphologies, i.e.: an extended and a compact flare. This energy range is crucial for the understanding of small flares and it might present different problems because of instrumental performances.

### 3.1. Extended flare

The minimum FOV to include all features of this complex-source flare is $128'' \times 128''$ (larger black box in Figure 1), centered on the point with solar coordinates (340,80), which seems to be the center of the
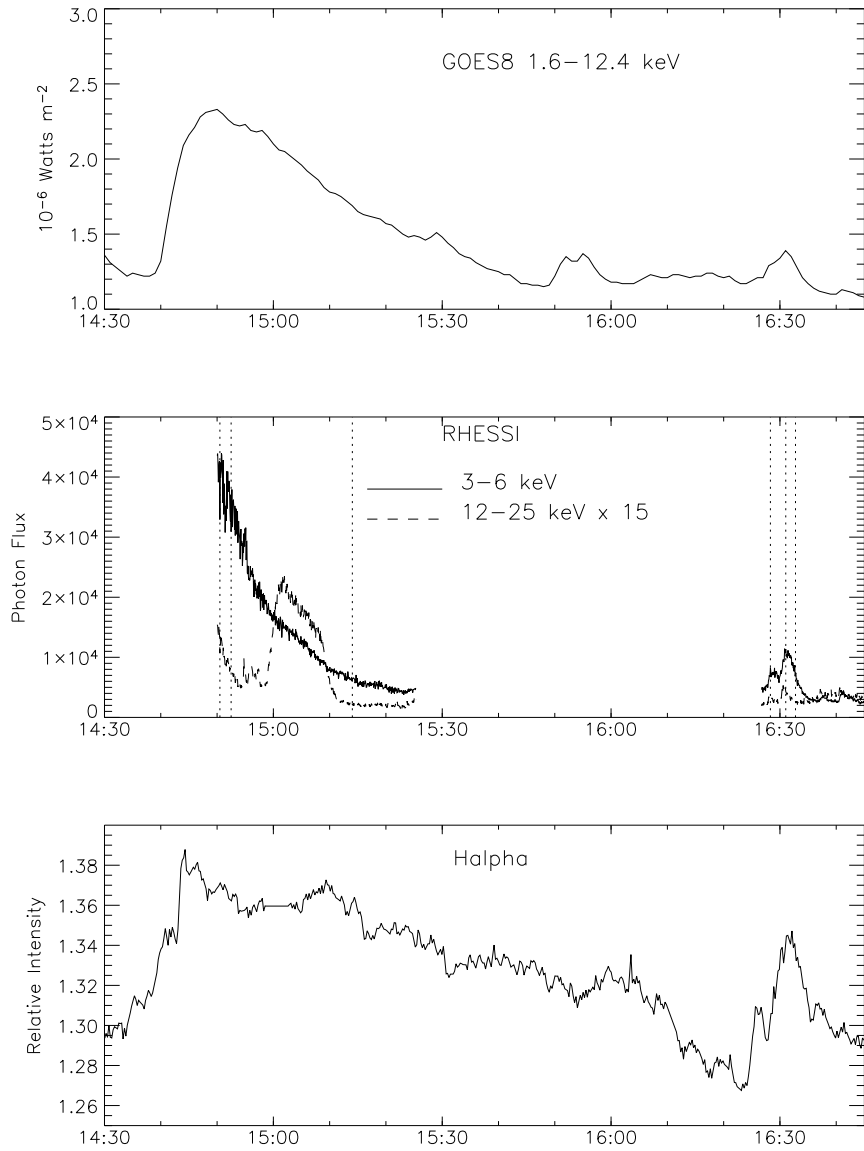
5

*Figure 3.* Light curves of the two flares observed by GOES (top), RHESSI (middle) and UBF (bottom). In the middle panel, the vertical dotted lines indicate the times at which both the RHESSI images and spectra have been studied. Notice the strong increase between 14:56 UT - 15:12 UT in the energy bin $12 - 25$ keV that is due to a particle precipitation event (see text).
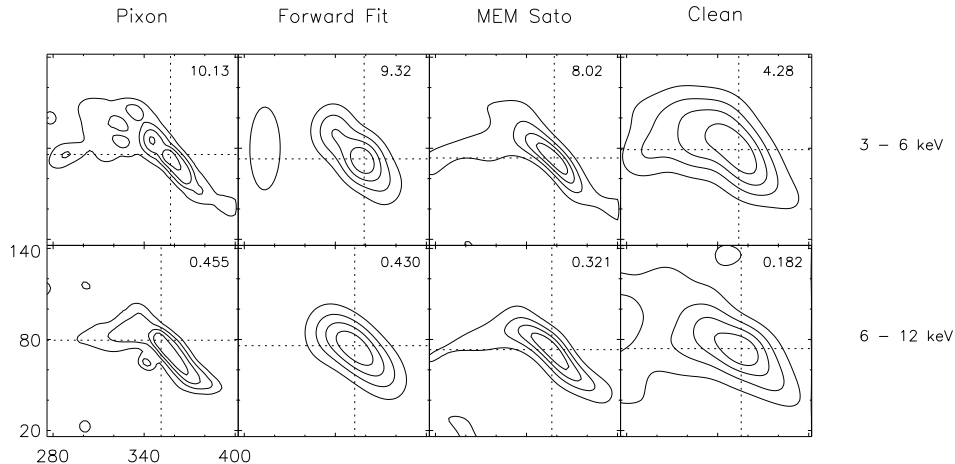
*Figure 4.* Extended flare: isocontours (20 %, 40 %, 60 %, 80 % of the peak intensity, indicated in the upper right corner) of the images reconstructed with four algorithms at 14:50:30 UT.

X-ray emission. We reconstructed the images with a pixel size of $2'' \times 2''$ considering a time interval $\Delta t = 60$ s which is short enough to give a low flux gradient at the considered time. We set off the time variability option (see later). The choice of collimators that contributed usefully to the definition of images has been accurate even if there is a certain arbitrariness.

Collimator 2 cannot be employed for imaging below 20 keV due to a failure during the early phases of the mission (Smith et al., 2002). We made separate back-projection images for each other collimator and discarded those which show no obvious source. At the end, we decided to use collimators 5 – 8 (FWHM of the lower grid = 20.4''). Collimator 9 (FWHM of 186'') is excluded, as its low resolution does not add any new features, given the field of 128''. Collimator 7 is also excluded in the 3 – 6 keV range because its energy threshold is 7 keV and its resolution is 3 keV. The reduced number of detectors used (only 3 over 9 in the 3 – 6 keV range) could raise concerns on the results of this comparative analysis. However, we will show in the next Sections that the source parameters are not strongly affected by the number of detectors used in the reconstruction process.

We compare the results obtained using four imaging algorithms available in the RHESSI data analysis software (*Pixon, Forward-fit, MEM-Sato, Clean*). We tried also the *MEM-Vis* algorithm but we could

Table I. Parameters obtained with different algorithms for the main source of the extended flare at 14:50:30 UT (see text for explanations).

| Algorithm | Energy | $x_p,y_p$ | $F_p$ | $F_{tot}$ | $w_x$ | $w_y$ | H/C |
|---|---|---|---|---|---|---|---|
| Pixon | 3-6 | 357.4,75.9 | 10.1 | 17362 | 35.0 | 20.9 | 0.30 |
| Forw. Fit | 3-6 | 359.0,73.0 | 9.3 | 18240 | 38.2 | 32.2 | 0.19 |
| MEM Sato | 3-6 | 358.3,73.6 | 8.0 | 16880 | 36.0 | 24.4 | 0.38 |
| Clean | 3-6 | 353.9,79.1 | 4.3 | 15000 | 64.1 | 46.8 | 0.24 |
| Pixon | 6-12 | 351.2,79.5 | 0.45 | 757.87 | 36.0 | 21.4 | 0.16 |
| Forw. Fit | 6-12 | 352.8,75.9 | 0.43 | 673.26 | 37.4 | 32.9 | 0.05 |
| MEM Sato | 6-12 | 356.7,73.3 | 0.32 | 735.80 | 35.9 | 29.2 | 0.26 |
| Clean | 6-12 | 355.5,74.0 | 0.18 | 678.92 | 60.0 | 42.9 | 0.25 |

not obtain the convergence for this method. Due to the complexity of the source, to obtain a good reconstructed image with *Forward-fit* we had to use 4 elliptical Gaussians.

We considered the three energy ranges $3-6$, $6-12$ and $12-25$ keV, but we had to exclude from our analysis the latter range, because the pileup effect is important for this flare (see Sect. 4.2). No correction for pileup is currently available for imaging, because the magnitude of the pileup varies on the same short timescales as the modulation, thus an exact correction for pileup would require an a priori knowledge of the image at all energies (Hurford, private communication).

In Figure 4 we show the contours of the images obtained with the different algorithms in the $3-6$ and $6-12$ keV range at 14:50:30 UT (all RHESSI times refer to the center of the adopted integration interval). The other selected times provide very similar results and are not presented here.

For each reconstructed image we give in Table I the parameters obtained in the $3-6$ and $6-12$ keV energy ranges, that might help to assess the stability and the congruity of the different methods:

- The peak position $x_p$ and $y_p$ (arcsec), found by a parabolic fit of the nine pixels surrounding the image peak, and the peak flux on the detector $F_p$ (photon s$^{-1}$ cm$^{-2}$ arcsec$^{-2}$).

- The total flux over the image on the detector $F_{tot}$ (photon s$^{-1}$ cm$^{-2}$).

- The equivalent widths $w_x$ and $w_y$ along the x and y direction give an indication of the linear dimension in arcsec and are defined following Aschwanden et al. (2004).

8

– The $[Halo]/[Core]$ flux ratio H/C, where $[Core]$ is the flux per unit surface in the part of the image inside of a circle centered on the peak emission with a radius $\simeq 1.5$ times the resolution of the finest grid used, and $[Halo]$ is the flux per unit surface in the part outside of it (Aschwanden et al., 2004).

The peak positions agree within few seconds of arc, $\approx$ 1-2 px, and the total fluxes agree within 20 %. The peak flux values and the linear dimensions $w_{x,y}$ differ more than a factor of 2: *Pixon* and *Forward-fit* give similar results while *Clean* finds the lowest value for the peak flux and the largest for the linear dimensions. This is however an expected result, because *Clean* does not deconvolve the source from the Point Spread Function (PSF) of the instrument. However, the flux integrated over the source ($F \approx F_p\, w_x\, w_y$) differs up to a factor of 1.5 and is not strictly conserved for different algorithms as in the case discussed by Aschwanden et al. (2004).

The $[Halo]/[Core]$ flux ratio indicates how much each method spreads the photons detected over the FOV outside the real sources. However, we stress that, especially in the case of a multiple-source flare, the $[Halo]$ takes into account also photons coming by other real sources present in the FOV. *Forward-fit*, as implicit in the hypotheses used to reconstruct the image, obtains the lowest value for this ratio. *MEM-Sato* finds a source size comparable to *Forward-fit* and *Pixon*, but it obtains the highest $[Halo]/[Core]$. Thus, we can say that *MEM-Sato* leaves more photons out of the source.

Finally, we investigate how the image reconstruction process is affected by the presence of unmodulated flux due to a combination of scattered flare photons within the instrument and a non-flare background flux (Aschwanden et al., 2004). *Pixon* and *Forward-fit* have options to detect and remove this component. The corrected images obtained with *Forward-fit* are very similar to the uncorrected ones giving variations of a few percent on the parameters reported on Table I. Instead, the parameters obtained with *Pixon* differ up to 40 % (if we exclude the total flux that is almost unchanged) giving very different results even in the peak position ($\Delta x_p = -8''$, $\Delta y_p = +9''$) while the general morphology of the emitting region appears to be unchanged.

The *Clean* algorithm has the possibility to correct the image for the residual map: this procedure strongly affects the total flux that decreases more than 20 % and then differs more than 40 % from values found with other algorithms. However, the $[Halo]/[Core]$ ratio decreases as well as the flux integrated over the source. This means that the correction for the residual map subtracts photons from the field of view, but mainly from the halo.
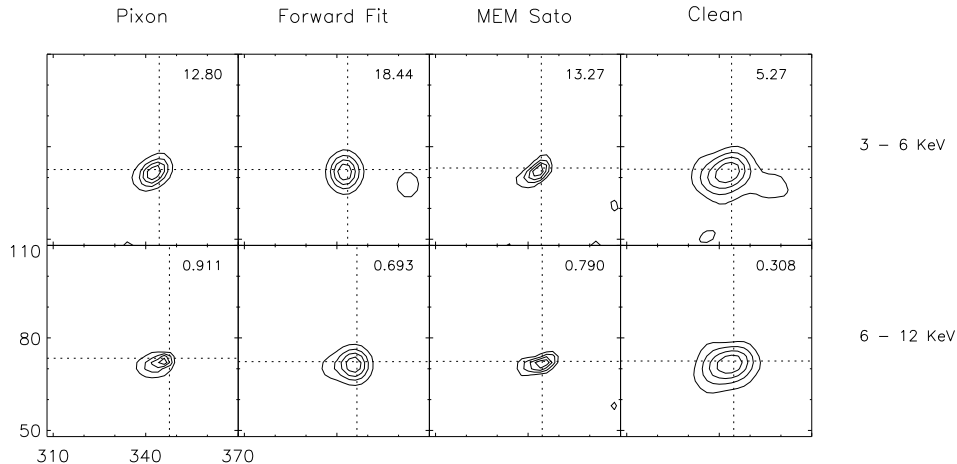
9

*Figure 5.* The same as in fig. 4 at 16:27:58 UT.

## 3.2. Compact flare

To reconstruct the images of this compact event we could use a FOV of $64'' \times 64''$ (smaller black box in Figure 1), centered on the point with solar coordinates (340,80), and a pixel size of $2'' \times 2''$. Since the light curve (Figure 3) shows rapid variations with two rise phases, two maxima and a decay phase, the time interval required for the image reconstruction should be short and we set $\Delta t = 20$ s. To create the images we used collimators $3 - 7$ with a FWHM $= 6.8''$ of the finest grid considered. Collimators $8 - 9$ were excluded, because their FWHM ($96''$ and $186''$ respectively) exceeds the FOV and collimator 7 was excluded in the range $3 - 6$ keV, as in the previous case. This flare has a simpler structure and we were able to use 2 elliptical Gaussians to reconstruct images with *Forward-fit* algorithm.

We examined the four imaging algorithms in different evolution phases of the flare with the time variability option switched off. The general behaviour of the algorithms does not change with the flare evolution and in Figure 5 we show as an example the images reconstructed in the first rising phase (16:27:48 UT – 16:28:08 UT) for the energy ranges $3 - 6$ and $6 - 12$ keV. In Table II the parameters obtained for these images are reported.

Analyzing the parameters given in Table II we see that the peak positions found with all algorithms agree very well within $2''$, and the total fluxes agree within 10 %, but only if we exclude the *Clean* algorithm.

10

Table II. Parameters obtained with different algorithms for the main source of the compact flare at 16:27:58 UT.

| Algorithm | Energy | $x_p,y_p$ | $F_p$ | $F_{tot}$ | $w_x$ | $w_y$ | H/C |
|-----------|--------|-----------|-------|-----------|-------|-------|-----|
| Pixon | 3-6 | 344.4,72.6 | 12.8 | 2023 | 10.1 | 9.5 | 0.11 |
| Forw. Fit | 3-6 | 343.5,72.8 | 15.0 | 2121 | 10.2 | 9.9 | 0.04 |
| MEM Sato | 3-6 | 344.3,73.1 | 13.3 | 1885 | 8.4 | 7.1 | 0.21 |
| Clean | 3-6 | 344.0,72.7 | 5.3 | 724 | 17.0 | 11.5 | – |
| Pixon | 6-12 | 347.7,73.4 | 0.9 | 77.21 | 10.2 | 9.7 | 0.05 |
| Forw. Fit | 6-12 | 346.5,72.3 | 0.7 | 67.37 | 10.4 | 9.7 | 0.004 |
| MEM Sato | 6-12 | 344.6,72.4 | 0.8 | 75.13 | 9.7 | 8.8 | 0.08 |
| Clean | 6-12 | 344.7,72.5 | 0.3 | 19.15 | 15.7 | 10.2 | – |

*Pixon* and *Forward-fit* give very similar results for the peak flux and the linear dimensions while *MEM-Sato* and *Clean* give different values resulting in a flux integrated over the source a factor of 2 lower. The image obtained with *Clean* shows actually very high negative residuals out of the main source: consequently the total flux over the FOV is much lower than that obtained with other algorithms and moreover the $[Halo]/[Core]$ ratio cannot be reliably computed. Even if we use the available option in order to correct the image for the residual map we cannot obtain more reliable results. As in the case of the extended flare the *MEM-Sato* algorithm gives the highest value of $[Halo]/[Core]$ ratio. Finally we use for *Pixon* and *Forward-fit* the options to remove the unmodulated flux: in this case the parameters change only of a few percent.

For both the extended and the compact flare we did some other tests to verify the stability of the parameters found. Changing the pixel size from $1''$ to $4''$ does not change the parameter values more than 1 %. A similar variation is obtained with the time variability option on and off, indicating that if the time interval considered is short enough to give a low flux gradient this option can be dropped. For the compact flare in the energy range $12 - 25$ keV, when the counts are very low, we could not obtain the convergence of any algorithm if we consider a $\Delta t = 20$ s, but we should use $\Delta t = 60$ s. Within this interval the counts are highly variable and to reconstruct an image it is mandatory to set the time variability option on.

We can conclude that in our two cases of small flares, the results obtained by different algorithms do not depend on the chosen energy band within the $3 - 12$ keV range even if the detector 7 has been excluded only in the $3 - 6$ keV band. This indicates that the reconstruction

algorithms are reliable even when only few collimators are useful to detect the emission source (see Sect. 3.1). Different algorithms may find different problems in reconstructing the images, but the problems seem not to be related to the extension or compactness of the source but rather to the complexity of the region.

*MEM-Sato* always gives the highest value for H/C as found by Aschwanden et al. (2004). However, in all the cases we examined it does not under-resolve the source, giving always linear sizes of the same order of the other algorithms. *Pixon* and *Forward-fit* give similar results but in the case of the extended flare the images reconstructed by *Forward-fit* do not seem to show the real complexity of the source. Thus we use *Pixon* to reconstruct the images for the analysis of flare evolution.

## 4. Spectra evolution

We analysed the spectral characteristics for the spatially integrated flux of our two flares as they evolve in time. The count spectrograms were created using the standard RHESSI software (updated April 2004). We used the front segments of the detectors in the $3 - 25$ keV energy range, with the energy binning set to 1/3 keV, excluding detectors 2 and 7, which have lower energy resolution (Smith, 2002a; Smith, 2002b). The full spectrum response matrix has been used to calibrate the data, and the SPEX code (Schwartz, 1996; Smith et al., 2002) has been used for the spectral fitting. We considered energies above 4 keV, because the lower energy intervals are not well calibrated yet. We tried to fit the observed count spectrum with three different models of photon spectrum:

- A single thermal bremsstrahlung emission whose best-fit parameters are the temperature T of the isothermal emitting plasma and its emission measure EM.

- A thermal plus a non-thermal bremsstrahlung emission whose best-fit parameters are, besides T and EM of the isothermal emitting plasma, the power law index $\gamma$ and the normalization of the power-law at the normalization energy fixed at 10 keV. We assume a power-law index fixed to 1.5 for energy below the energy cutoff, that is determined as the one that gives the lowest $\chi^2$ value (see Sec. 4.3). We recall that $\chi^2$ is the reduced one, computed considering the numbers of free parameters.

- A double thermal bremsstrahlung emission that assumes the presence of two isothermal components and gives as best-fit parameters
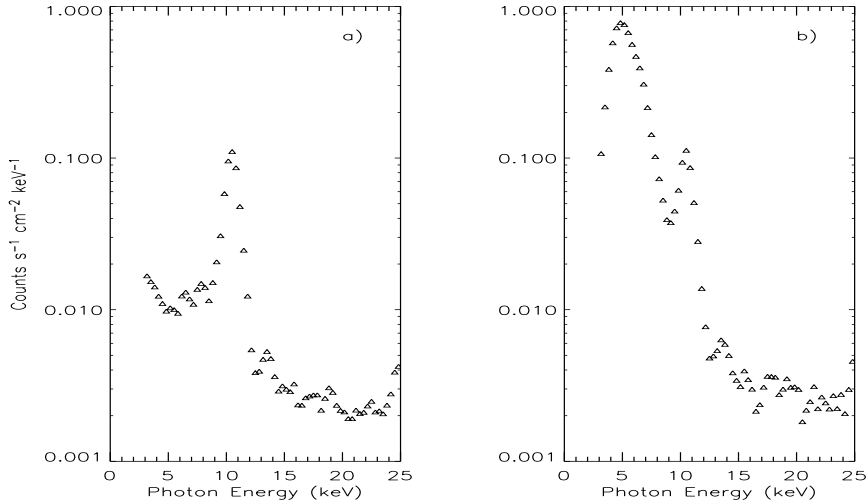
12

*Figure 6.* (a) Count spectrum of the night background. (b) Count spectrum of the post-flare background. The spectra are significantly different only for energies $E \leq 8$ keV.

the temperatures T and $T_h$ and the emission measures EM and $EM_h$, for the cold and the hot component, respectively.

### 4.1. Choosing the background

RHESSI is a high-background instrument and the background selection in the spectra analysis is crucial in particular for small and low-energy flares. We considered two background spectra: the night background obtained averaging over few minutes before RHESSI exits the night for each flare, and the post-flare background determined between 16:55:30 - 16:57:30 UT, well after the decay of any flare. The night background, which includes all the instrumental contributions, represents a sort of lower limit, while for the post-flare background we point out that the chosen interval is more than two hours (and, in RHESSI terms, more than an orbit) far from the first flare, and almost half an hour from the second one.

In Figure 6 we compare the two background spectra. We can see that the post-flare background is at least one order of magnitude higher than the night background for energy lower than 8 keV, while the spectra are almost identical at higher energies. The two peaks at around 10.5 keV and 13.5 keV, present in both spectra, are probably due to the activation of the germanium detectors. We then expect the choice of the background will affect the flux spectra only at low energies.
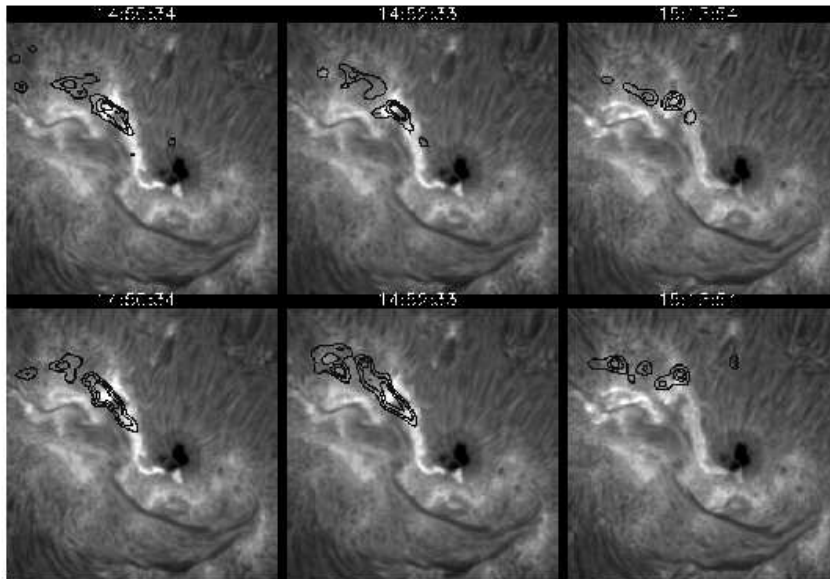
13

*Figure 7.* Evolution of the extended flare during the decay phase. Images in the Hα line center with overplotted isocontours (40 %, 60 %, 80 % of the peak intensity) of RHESSI images in the 3 – 6 keV (*top*) and 6 – 12 keV (*bottom*), obtained using *Pixon* algorithm.

## 4.2. SPECTRA OF THE EXTENDED FLARE

In Figure 7 we show the evolution of the extended flare during its decay phase. The RHESSI images are obtained using *Pixon* algorithm with detectors 3 – 8 (excluding detector 7 in the 3 – 6 keV band, see Sect. 3.1 ) and $\Delta t = 60$ s. We could select all available collimators because *Pixon* decides which ones to keep and which to discard. The precision of the alignment between Hα and RHESSI images is estimated to be around 5″. Hα images show the decreasing intensity of the ribbon. At 14:50:30 UT the RHESSI emission maximum coincides with the loop footpoints outlined by the Hα west-ribbon and only a weak emission is present in the northern part of the FOV tracing the inferred large loop system connecting the two ribbons visible in Figure 1. Enlarging the RHESSI FOV we found that, from this time on, no X-ray emission is present in the eastern ribbon location. During the decay the intensity of Hα footpoints decreases as well as the peak flux of RHESSI images (variations are within a factor 10) and the X-ray maximum emission moves from the footpoints to the loop top.

At least up to 14:53 UT the counts are $\geq 2000$ count s$^{-1}$ per detector, which is the estimated threshold for the presence of *pileup* effect
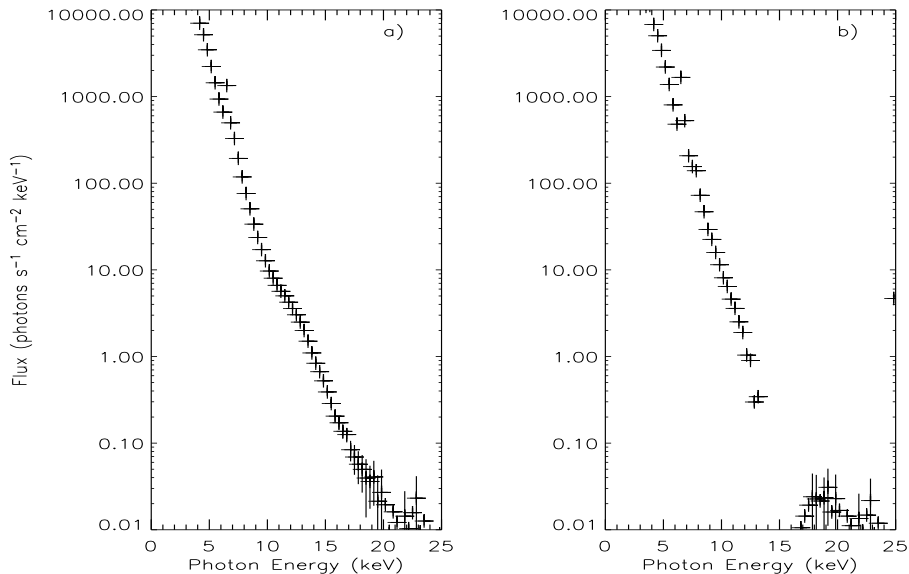
*Figure 8.* 14.50.30 UT (a) Energy spectrum after the background subtraction with no pileup correction: the feature between $\approx 10 - 15$ keV is due to pileup. (b) The spectrum after the pileup correction.

when both attenuators are out (Smith, 2002a). When pileup occurs multiple photons are recorded as a single photon with an energy equal to the sum of energies of the individual photons. In Figure 8 we show the spectrum before and after the correction for the pileup. While the correction works properly below 12 keV, at higher energies the spectrum seems overcorrected. Usually the pileup is present for large flares and affects particularly the $20 - 50$ keV energy range, and the error for its correction is estimated of about 20 % when the spectrum is flat (Smith, private communication). In our energy range the spectrum is very steep and the error could be much higher. The clear presence of pileup in the spectrum prevents us to reconstruct reliable images in the $12 - 25$ keV range.

Hence we decided to fit the spectra in the energy range $4 - 10$ keV using the same time intervals of the images. Contrary to expectations, the background choice does not strongly affect the resulting parameters even in the low energy part of the spectrum, probably because of the high counts recorded for this flare. In table III we give the parameters for the 3 models of the photon spectrum, obtained subtracting the post-flare background spectra (see Sec. 4.1). At 14:50:30 UT and 14:52:30 UT the single thermal model fitted the observed spectra giving a high $\chi^2$ of about 4 while the other two models fitted the spectra with low

15

Table III. Parameters obtained fitting the spectra with 3 models during the decay phase of the extended flare. EM, $EM_h$, T and $T_h$ are the emission measure and the temperature, respectively, of the cold and hot thermal components, $\gamma$ is the exponent of the power-law for the non-thermal component. The $\chi^2$ value is also given.

| UT | model | EM $(10^{48}$ cm$^{-3})$ | T MK | $\gamma$ | $EM_h$ $(10^{48}$ cm$^{-3})$ | $T_h$ MK | $\chi^2$ |
|---|---|---|---|---|---|---|---|
| 14:50:30 | th. | 1.0 | 12 | | | | 3.7 |
| | th + non th. | 1.7 | 10 | 10 | | | 2.4 |
| | double th. | 1.7 | 9 | | 0.24 | 14 | 2.4 |
| 14:52:30 | th. | 1.2 | 11 | | | | 3.5 |
| | th + non th. | 2.1 | 10 | 11 | | | 1.9 |
| | double th. | 2.0 | 9 | | 0.10 | 14 | 2.1 |
| 15:14:00 | th. | 0.8 | 8 | | | | 1.2 |

comparable $\chi^2$ values of about 2. For the non-thermal model we set the cutoff at 7 keV (see Sec. 4.3 for the discussion on the best choice of cutoff value) and we obtain a very steep power-law index $\gamma \approx 10$, as found in the decay phase of some RHESSI microflares (Krucker et al., 2002, Hannah et al., 2004). For the double thermal model the hot component has a temperature of about 14 MK, compared with the 9 MK of the 'cold' component.

At 15:14 UT instead, when the footpoint emission is decreased and the contribution of the loop top increases, the single thermal model adequately fits the spectrum (T = 8 MK and EM = $0.8 \times 10^{48}$ $cm^{-3}$) reaching a $\chi^2$ of about 1. This is coherent with the scenario of an eruptive two-ribbon flare characterized by a global magnetic field disruption and processes of energy release long lasting after the impulsive phase. The magnetic reconnection process, responsible for these energy release episodes, is very fast in the beginning of the flare and slows down in later phases (Carmichael, 1964, Sturrock, 1966, Hirayama, 1974, Kopp and Pneuman, 1976). We can postulate that at 15:14 UT there are no more energy release episodes and thus, when the footpoints of the loop do not contribute significantly to the total emission, the plasma emission is only thermal.

### 4.3. Spectra of the compact flare

The RHESSI images are obtained using the *Pixon* algorithm with detectors 3 – 7 (the detector 7 is not included in the 3 – 6 keV band). In the range 3 – 12 keV we considered $\Delta t = 20$ s, while in 12 – 25 keV
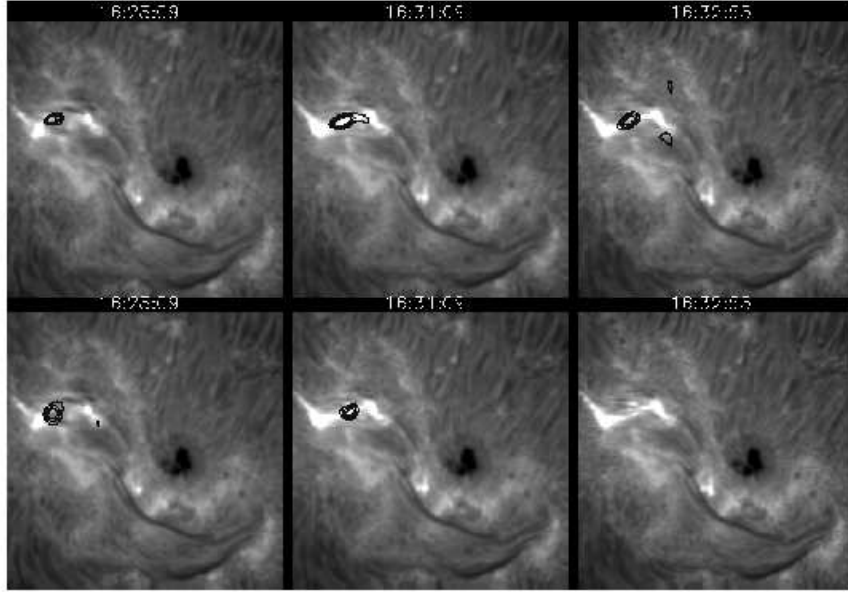
*Figure 9.* Evolution of the compact flare. Images in the Hα line center with over-plotted isocontours (40 %, 60 %, 80 % of the peak intensity that changes within a factor 5) of RHESSI images in the $6-12$ keV (*top*) and $12-25$ keV (*bottom*). The images are obtained using *Pixon* algorithm with $\Delta t = 20$ s and 60 s, respectively. At 16:32:53 no reliable image can be reconstructed in the $12-25$ keV energy range due to the low counts.

we had to consider $\Delta t = 60$ s (see Sec. 3.2). In Figure 9 we show the evolution of the compact flare beginning with the rise phase observed by RHESSI (times are indicated in Figure 3). The RHESSI contours are very similar in $3-6$ keV and $6-12$ keV energy bins and we show only $6-12$ keV and $12-25$ keV contours. Hα images show that the bright features develop with time along the filament which is well visible before and after the flare (see Figure 2). Also the contours of RHESSI images in the $6-12$ keV energy band change with time following the direction of the filament. In the $12-25$ keV the peak emission moves along the filament and the contours, elongated in the North - South direction, probably include the loop footpoints and suggest the presence of low loops crossing the filament.

We fit the spectra obtained with $\Delta t = 20$ s. Since no pileup effect is present in this flare, the data are reliable in the energy range $4-25$ keV. We fit the spectra changing the energy range from $4-10$ keV to $4-25$ keV and we see that the found parameters change within 1 % while the $\chi^2$ decreases by a factor of two increasing the range of energy.
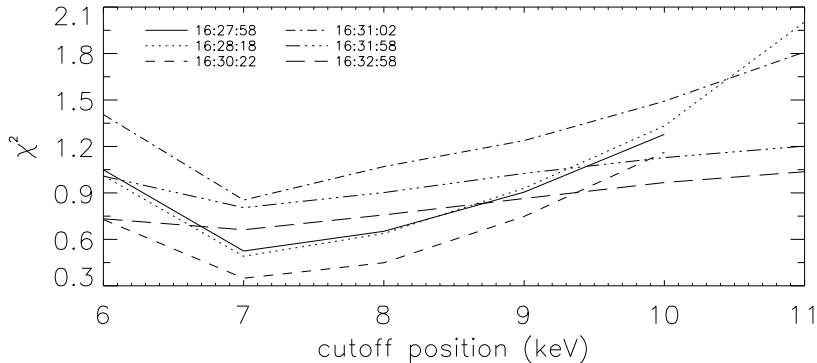
17

*Figure 10.* $\chi^2$ vs. the non-thermal energy cutoff value at different times during the flare.

With the single thermal model the fit provides high $\chi^2$ values ($\approx$ $6 - 8$) with high residuals at energies $\geq 10$ keV. To fit the observed data adding a power-law non-thermal spectrum at first we analyze the output parameters changing the position of the energy cutoff from 6 keV to 11 keV. The found $\gamma$ index can vary up to 15 % with random residuals. The resulting $\chi^2$ seems to depend on the energy cutoff as shown in Figure 10 at different times during the flare. The minimum value is always reached with a cutoff between 7 keV and 8 keV, so we adopted 7 keV as the standard value for the cutoff. A posteriori, we can justify the use of the data in the $4 - 10$ keV range to fit the spectrum and the setting of the cutoff of the non-thermal model at 7 keV also for the first flare, when the pileup effect makes unreliable the high energy data.

In Figure 11 we show, as an example, the spectra at the time of the second peak (16:30:52 UT – 16:31:12 UT) fitted with different models. The broadened emission feature at around 6.7 keV, corresponding to a group of emission lines mainly due to Fe XXV and Fe XXVI, is also taken into account by the SPEX code in the fitting procedure. Phillips (2004) warned about the fact that SPEX computations are based on ionization and recombination data that overestimated the fraction of Fe XXV at T $\approx$ 10 MK.

As expected, the choice of background for this very weak flare heavily affects the parameters of the cold thermal spectrum: the EM obtained subtracting the night background is approximately twice the EM obtained with the post-flare background while the temperature is on the average 0.5 MK lower. On the contrary the fitting parameters that characterize the power-law or the hot components are not substantially
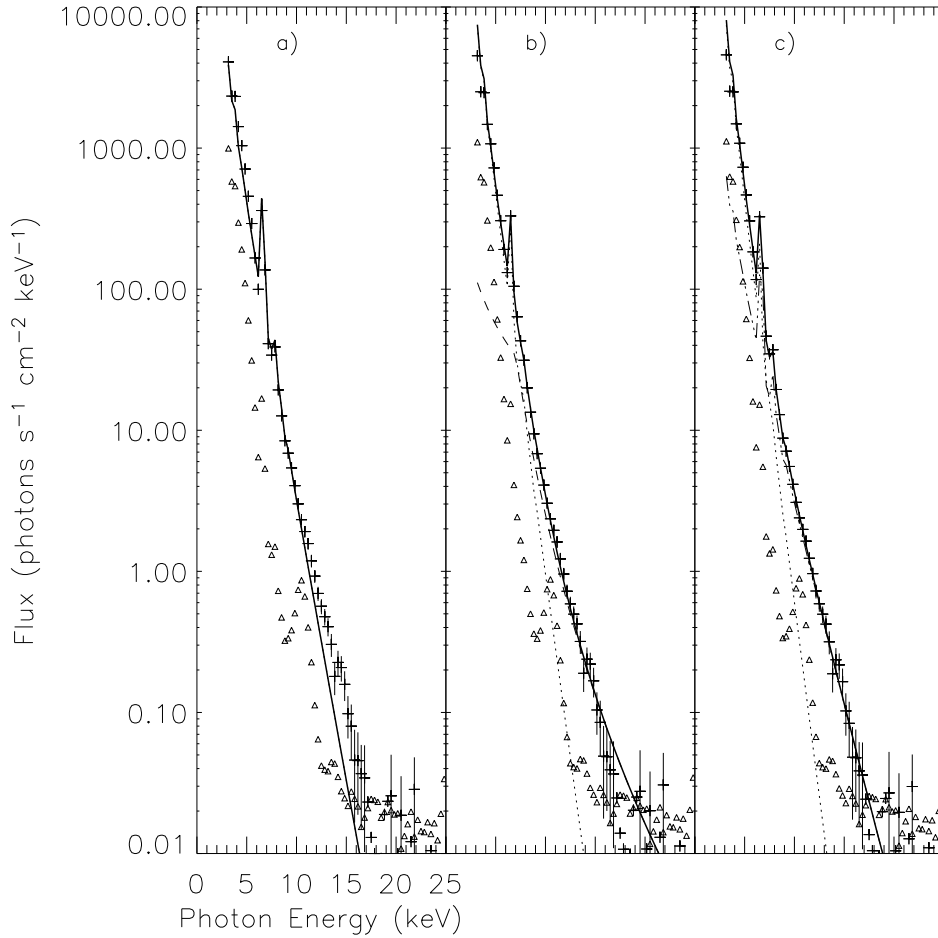
18

*Figure 11.* Fitting of the observed spectra (crosses) at 16:31:02 UT with the 3 considered models. The triangles indicate the background. The result of the fit is indicated by the *solid line* and the thermal component by the *dotted line.* (a) Single thermal model. (b) Thermal plus non-thermal model (*dashed line*). (c) Double thermal model (the hot component is indicated by the *dot-dashed line*).

altered by the background as was also found by Qiu et al. (2004). In table IV we give the parameters obtained for the 3 models taking into account the post-flare background spectra (see Sec. 4.1). In the rise and peak phases of the flare the non-thermal spectrum has a $\gamma$ of about 7 while in the decay phase $\gamma$ increases up to 10, as in the decay phase of the other flare. The high value of $\gamma$ reached when the emission decreases, indicates a softening of the emission with respect to the peak phase. If we assume a double thermal model, the hot component is always

Table IV. Parameters obtained fitting the spectra with 3 models during different phases of the compact flare. EM, $EM_h$, T and $T_h$ are the emission measure and the temperature, respectively, of the cold and hot thermal components, $\gamma$ is the exponent of the power-law for the non-thermal component. The $\chi^2$ value is also given.

| UT | model | EM ($10^{48}$ cm$^{-3}$) | T (MK) | $\gamma$ | $EM_h$ ($10^{48}$ cm$^{-3}$) | $T_h$ (MK) | $\chi^2$ |
|---|---|---|---|---|---|---|---|
| 16:27:58 | th. | 0.08 | 12 | | | | 5.0 |
| | th. + non th. | 0.24 | 9.7 | 7.7 | | | 0.6 |
| | double th. | 0.32 | 8.9 | | $6.0\ 10^{-3}$ | 20 | 0.5 |
| 16:28:18 | th. | 0.11 | 12 | | | | 4.3 |
| | th. + non th. | 0.26 | 10 | 7.7 | | | 0.5 |
| | double th. | 0.32 | 9.4 | | $7.5\ 10^{-3}$ | 19 | 0.5 |
| 16:30:22 | th. | 0.07 | 14 | | | | 7.7 |
| | th. + non th. | 0.31 | 9.9 | 7.2 | | | 0.5 |
| | double th. | 0.43 | 9.0 | | $7.0\ 10^{-3}$ | 21 | 0.4 |
| 16:31:02 | th. | 0.09 | 14 | | | | 6.4 |
| | th. + non th. | 0.33 | 11 | 7.3 | | | 0.9 |
| | double th. | 0.39 | 10 | | $9.1\ 10^{-3}$ | 21 | 0.5 |
| 16:31:58 | th. | 0.21 | 12 | | | | 2.5 |
| | th. + non th. | 0.37 | 10 | 8.2 | | | 0.8 |
| | double th. | 0.41 | 9.7 | | 0.010 | 17 | 0.8 |
| 16:32:58 | th. | 0.25 | 10 | | | | 1.3 |
| | th. + non th. | 0.41 | 9.0 | 10.6 | | | 0.6 |
| | double th. | 0.42 | 8.9 | | $4.8\ 10^{-3}$ | 16 | 0.7 |
| 16:34:02 | th. | 0.27 | 8.7 | | | | 1.2 |

present during the flare and has a temperature T ≈ 20 MK (compared to 10 MK of the cold one) and an EM two orders of magnitude lower than that of the cold component. The temperature we found is anyway quite lower than the 35 MK indicated for the so called "superhot" component first identified by Lin et al. (1981) and afterward defined as the component giving rise to the Fe XXVI emission lines observed in large flares with BCS on Yohkoh (see e.g. Pike et al., 1996).

4.4. DISCUSSION

An important result is that, for both flares, only towards the end of the decay phase the best fit can be obtained with a thermal photon spectrum while during the flare the best fit can be obtained, with comparable $\chi^2$ values, adding either a non-thermal component or a hot thermal component. The two models are equivalent on this sta-

20

tistical base and it is difficult to select the best model to interpret the observations. We try to use the Fe line feature at 6.7 keV, well visible in our observed spectra, to choose between these two models. Phillips (2004) computed synthetic spectra using the CHIANTI code and found that this feature becomes visible above the continuum only when T $\geq$ 10 MK (with an EM = $10^{49}$ cm$^{-3}$). Its equivalent width gives the best temperature diagnostic reaching a value of 3 keV for temperature T $\approx$ 20 MK. We measured the equivalent width of this line in the count spectra and we found a value always $\leq$ 1.0 keV that indicates a thermal plasma with T $\leq$ 12 MK. We hence believe that the observed spectra could be better interpreted adding a non-thermal spectrum to a thermal one.

From the fit parameters we can compute the thermal and the non-thermal contribution to the flare energy budget, assuming that the accelerated electrons lose their energy primarily through Coulomb collisions in the thick target approximation (Lin et al., 2001):

$$E_{th} = 3k_B T \sqrt{EM\, V} \qquad (1a)$$

$$E_{non-th} = 9.5 \times 10^{24} \gamma^2 (\gamma - 1) B(\gamma - 1/2, 3/2) A E_0^{-(\gamma-1)} \Delta t \qquad (1b)$$

where $k_B$ is the Boltzmann constant, T and $EM$ the temperature and the Emission Measure of the thermal part, V the volume of the source, $B(a,b)$ the standard beta function, $A$ the normalization factor of the photon spectrum, $E_0$ the energy cutoff, and $\Delta$t the time interval. T, $EM$, $\gamma$ and $A$ are derived from the fitting. We estimated $V$ from the flare size (see $w_{x,y}$ in Table II). For the extended flare we have observations only during the decay phase and we find $E_{th} \approx 1 \times 10^{30}$ erg and $E_{non-th} \approx 1 \times 10^{31}$ erg. For the compact flare we find that both $E_{th}$ and $E_{non-th}$ are approximately constant during the flare with $E_{th} \approx 5 \times 10^{28}$ erg and $E_{non-th} \approx 5 \times 10^{29}$ erg. Thus, the non-thermal energy is higher than the thermal energy by about a factor 10 not only in the rise and peak phases of the second flare but also during the decay phase of both flares. The high value of the $\gamma$ index in this phase, that indicates a softening of the emission, balances the low value of the normalization factor of the photon spectrum $A$. This means that the non-thermal electron energy is the energy supply for the heating of the thermal plasma. This result can thus be considered an a posteriori support to the non-thermal model choice.

## 5. Conclusions

We use RHESSI data and ground based observations to study two small flares (GOES class C1 and C2) developed in the same active region with different characteristics: the first is a two-ribbon extended flare implying high coronal loops while the other is a compact two ribbon implying low-lying loops. This is reflected in RHESSI imaging at different energies that outline the loop morphology in the two cases.

We analyzed the accuracy of different algorithms implemented in the RHESSI software to reconstruct the image of the emitting sources, for energies (between 3 and 12 keV) that are particularly important when studying microflares. We found that all tested algorithms give similar results for the peak positions and the total flux on the considered FOV, as found by Aschwanden et al. (2004) for higher energies. The peak flux values and the linear sizes differ at most by a factor 2. *Clean* gives always the lowest peak and the largest size (does not deconvolve from the PSF of the instrument) while the other algorithms give very similar results. *Clean* can give additional problems even if the flare structure is simple. In fact for our compact flare it shows very high negative residuals out of the main source and then does not conserve the total flux over the FOV. The available option to correct for residual map does not help to solve the problem. *MEM-Sato* always gives the highest value for H/C, i.e. tends to spread more photons out of the source than the other methods, as found by Aschwanden et al. (2004). *Pixon* and *Forward-fit* do converge to similar results. Both algorithms have the option to detect and remove the unmodulated flux present in RHESSI data. *Forward-fit* finds a unmodulated component that slightly changes the source parameters for both flares, while in the case of extended complex flare, *Pixon* finds a component that strongly changes the source parameters. On the other hand, *Forward-fit* is not able to reproduce the real complexity of the source, hence we used *Pixon* (without background correction) to reconstruct the images of the two flares during their evolution. In fact, while the reliability of *Pixon* is not surprising, the most relevant result of our study is that each other method can meet significant problems, and special care is always required employing them. In any case, we outline the importance of comparing different algorithms when analyzing events in order to establish whether the reconstructed features are real or not.

We studied the spectral characteristics of our flares by fitting the count spectra with 3 different models of photon spectrum: a single isothermal spectrum, an isothermal plus a non-thermal spectrum and a third one with two isothermal components. The photon spectrum seems to depend on the flare phase. The single thermal model is adequate to

fit the observations only during the very final decay phase. During the flare, instead, the single thermal model provides $\chi^2$ values a factor of 10 higher than the one obtained with the other two models. The non-thermal and the double thermal fits are comparable, and the choice between them can not rely on statistics. The measured equivalent width of the Fe line feature at 6.7 keV is low compared to that expected for a plasma at 20 MK. Although further investigation is necessary, this may suggest that the hot thermal component is not relevant to the total emission. For the non-thermal spectrum we determined the energy cutoff value at 7 keV as the one that gives the lowest $\chi^2$ in the fitting. For the rise and peak phase we found a photon spectral index of 7 – 8, quite high for standard flares, but not so uncommon in microflares (Krucker and Hudson, 2004, Hannah et al., 2004), while during the decay phase $\gamma$ increases up to 10, indicating a softening of the emission with respect to the peak phase. With such a steep spectrum and a low energy cutoff the non-thermal energy contribution to the energy budget of the flare is always higher than the thermal one and perhaps the non-thermal electrons provide the energy for heating the thermal plasma through collisional loss.

As a "by-product" of our spectral study, we found that the pileup effect, usually observed during large flares, must be taken into account also for weak flares and that the correction enabled in the RHESSI software can give serious problems for the recovering of the spectra in the 3 – 25 keV energy range. We want to stress that the presence of pileup also affects the image reconstruction process, yielding unreliable images, because the photon energies are uncertain.

# References

Aschwanden, M.J., Schmahl, E., and the RHESSI team, 2002, *Solar Phys.* **210**, 193.

Aschwanden, M.J., Metcalf, T.R., Krucker, S., Sato, J., Conway, A.J., Hurford, G.J. and Schmahl, E.J.: 2004, *Solar Phys.* **219**, 149.

Benz, A.O. and Grigis, P.C.: 2002, *Solar Phys.* **210**, 431.

Carmichael, H. 1964, in 'The Physics of Solar Flares', ed. W. N. Hess (NASA SP-50) (Washington: NASA), 451

Fletcher, L. and Hudson, H.S.: 2002, *Solar Phys.* **210**, 307.

Grigis, P.C. and Benz, A.O.: 2004, *Astron. and Astrophys.* **426**, 1039.

Hannah, I. G., Christe, S., Krucker, S., Hudson, H. S., Fletcher, L., & Hendry, M. A. 2004, in *Soho 15, Coronal heating*, ed. D. Danesy, St. Andrews, UK. ESA SP-575, p. 259.

Harrison, R.A., Sawyer, E.C., Carter, M.K., Cruise, A.M., Cutler, R. M., Fludra, A., et al.: 1995, *Solar Phys.* **162**, 233.

Hirayama, T.: 1974, *Solar Phys.*, **34**, 323

Hudson, H.S. and Fárník, F.: 2002, in A. Wilson (ed.), *Solar variability: from core to outer frontiers.* The 10th European Solar Physics Meeting, 9 - 14 September 2002, Prague, Czech Republic. ESA SP-506, p. 261.

Hurford, G. J., Schmahl, E. J.,Schwartz, R. A., Conway, A. J., Aschwanden, M. J., Csillaghy, A., Dennis, B. R., Johns-Krull, C., Krucker, S., Lin, R. P., McTiernan, J., Metcalf, T. R., Sato, J., Smith, D. M.: 2002, *Solar Phys. 210*, 61.

Kopp, R. A. and Pneuman, G. W., 1976, *Solar Phys.* **50**, 85

Krucker, S., Christe, S., Lin, R.P., Hurford, G.J. and Schwartz R.A.: 2002, *Solar Phys.* **210**, 445.

Krucker, S., Hudson, H. 2004, in *Soho 15, Coronal heating*, ed. D. Danesy, St. Andrews, UK. ESA SP-575, p. 247.

Lin, R. P., Schwartz, R. A., Pelling, R. M., Hurley, K. C., 1981 *Astrophys. J.***251**, L109.

Lin, R. P., Feffer, P. T., Schwartz, R.A., 2001, *Astrophys. J.* **557**, L125.

Lin, R.P., et al., 2002, *Solar Phys. 210*, 1.

Liu, C., Qiu, J., Gary, D. E., Krucker, S. and Wang, H.: 2004, *Astrophys. J.* **604**, 442.

Metcalf, T. R., Hudson, H. S., Kosugi, T., Puetter, R. C., Pina, R. K, 1996, *Astrophys. J.* **466**, 585

Phillips, K.J.H: 2004, *Astrophys. J.* **605**, 921.

Pike, C. D., Pillips, K. J. H., Lang, J., et al., 1996, *Astrophys. J.***464**, 487.

Qiu, J., Liu, C., Gary, D. E., Nita, G. M. and Wang, H.: 2004, *Astrophys. J.***612**, 530.

Scherrer, P.H., Bogart, R.S., Bush, R.I., et al.: 1995, *Solar Phys.* **162**, 129.

Schwartz, R.A.: 1996, in *Compton Gamma Ray Observatory Phase 4 Guest Investigator Program: solar Flare Hard X-ray Spectroscopy*, Technical Report, NASA Goddard Space Flight Center.

Schwartz, R. A., Csillaghy, A., Tolbert, A. K., Hurford, G. J., McTiernan, J., Zarro, D., 2002, *Solar Phys.* **210**, 165.

Smith, D.M.: 2002a, 'Behind, Beneath and Before RHESSI Spectroscopy', from *RHESSI* website

Smith, D.M.: 2002b, 'Problems, Peculiarities, and Phenomena in RHESSI Spectroscopy', from *RHESSI* website

Smith, D.M., Lin, R.P., Turin, P. et al.: 2002, *Solar Phys.* **210**, 33.

Sturrock, P. A.: 1966, *Nature*, **211**, 695